Bi electrodeposition on WO_3 photoanode to improve the photoactivity of the $WO_3/BiVO_4$ heterostructure to water splitting

Dyovani Coelho[a,*], João Pedro R.S. Gaudêncio[a], Saulo A. Carminati[b], Francisco W.P. Ribeiro[c], Ana F. Nogueira[b], Lucia H. Mascaro[a,*]

[a] Federal University of São Carlos (UFSCar), Nanostructured Materials Laboratory Manufactured Electrochemically, Department of Chemistry, São Carlos 13565-905, Brazil
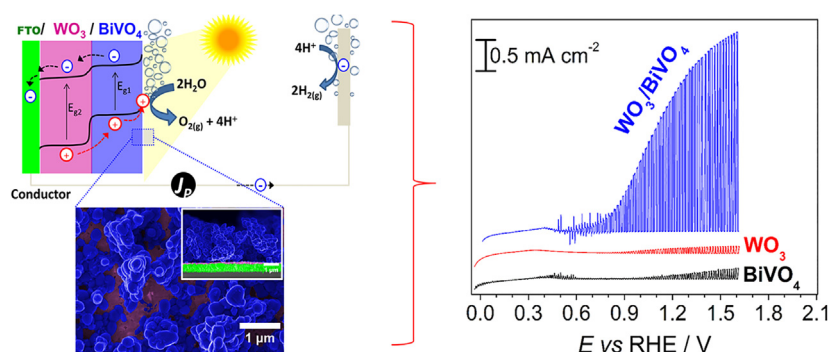[b] University of Campinas (UNICAMP), Laboratório de Nanotecnologia e Energia Solar, Chemistry Institute, Campinas 13083-970, Brazil
[c] Federal University of Cariri, Institute of Educators Training, Brejo Santo 63260-000, Brazil

HIGHLIGHTS

- Metallic Bi electrodeposition as a pre-step to improve the heterojunction $WO_3/BiVO_4$.
- Obtaining pillar-like $BiVO_4$ structure by intermediary step of Bi electrodeposition.
- Using spray, electrodeposition and drop-casting to build $WO_3/BiVO_4$ heterojunctions.
- Increasing the time constant of charge carriers by suitable heterojunction formation.

GRAPHICAL ABSTRACT

ARTICLE INFO

ABSTRACT

In view of the urgency to replace fossil fuel-based energy sources with sustainable and renewable sources, much has been done to discover new materials and/or production methods that can provide devices capable of converting solar energy into chemical or electrical energy. This work describes the electrodeposition of Bi on WO_3 film and its subsequent conversion to $BiVO_4$ with the addition of NH_4VO_3 and heat treatment. In this way, a $WO_3/BiVO_4$ heterojunction is obtained. With this methodology, it is possible to observe the formation of $BiVO_4$ nanostructures with pillar shapes and a photocurrent increase of 300 times compared to films obtained by drop-casting. At 1.23 V *vs* RHE (Reversible Hydrogen Electrode), the photocurrent achieved with the photoanode reaches 2.1 ± 0.3 mA cm^{-2}, which is 35 times higher than pure $BiVO_4$ and 23 times higher than pure WO_3. Transient absorption spectroscopy studies show an increase in the time constants for the recombination of charge carriers to the $WO_3/BiVO_4$ heterojunction. Electrodeposition is a relatively simple, easy to use, and scalable technique. So, it is expected that its use for the production of photoelectrodes will be more widespread.

1. Introduction

The use of a single semiconductor to complete water splitting and generate O_2 and H_2 is the main goal of the research, but the characteristics of the bandgap energy, valence, and conduction band positions and the incident photon-current conversion efficiency (IPCE) are not meeting the needs for a simple device [1]. Even in 2020, laboratories around the world are seeking photocatalysts for O_2 evolution that are inexpensive, efficient, and sustainable. The oxidation of water to evolve O_2 is the limiting reaction in water splitting due to its many reaction steps, i.e., a four-electron transfer coupled with the removal of four protons to produce a strong oxidizing medium [2–4]. In this context, $BiVO_4$ is considered a promising semiconductor due to its bandgap energy and valence and conduction bands suitable for this purpose. The monoclinic scheelite $BiVO_4$ phase presents a bandgap of ~ 2.45 eV, and its valence band is appropriate for water oxidation [5–8]. However, $BiVO_4$ has low electrical conductivity, charge carrier mobility, and hole diffusion length, which increase the recombination of photogenerated charges [9]. In spite of this, the production of heterojunctions has improved the photocatalysts properties of this devices [10].

The formation of heterojunctions is an alternative way to increase the IPCE of the materials used as photoanodes. The heterojunction is built up from close physical contact between two different semiconductors in such a way that there is a crystalline continuity in the locus of contact [11]. The crystalline continuity in the locus of physical contact causes a band alignment, which is lost as it moves away from the junction between semiconductors until the band position goes back to the characteristics of the bulk semiconductors. Additionally, there is an alignment in the band boundaries by the band-edge discontinuity [12]. This affects charge transport because it generates a charge transfer cascade between the semiconductor bands by the internal electric field. This phenomenon maximizes the charge separation and minimizes the recombination of the electron-holes pairs [13,14]. Besides, band level engineering is important for deciding on the semiconductor materials and the application of the device.

Most heterojunctions based on $BiVO_4$ use WO_3 as the semiconductor junction in a staggered gap configuration [15]. The bandgap of WO_3 is approximately 2.78 eV, and its conduction and valence band positions are lower energy than the analogous $BiVO_4$. This heterojunction design facilitates electron transfer from the $BiVO_4$ conduction band to the WO_3 conduction band and the hole transfer from the WO_3 valence band to the $BiVO_4$ valence band. Consequently, the holes accumulate at the $BiVO_4$ surface while the electrons accumulate at the opposite WO_3 surface, and the efficiency of charge separation increases. The increase of the charge separation using the staggered gap heterojunction based on $WO_3/BiVO_4$ has demonstrated relative success in water splitting devices [8,16–19]. The methods to produce the heterojunctions based on $WO_3/BiVO_4$ are shown in the Table 1. In all methods, there are annealing steps at temperatures above 450 °C to obtain the photoactive crystalline phases of the WO_3 and $BiVO_4$.

Although the electrochemical deposition of $BiVO_4$ is an interesting alternative because it is a scalable, inexpensive, and an easy technique, it has been barely investigated for this purpose. Direct $BiVO_4$ electrodeposition was studied by Seabold et al. [39] using an acetate buffer electrolyte containing $Bi(NO_3)_3$ and $VOSO_4$ at 70 °C pH 4.7 at 1.9 V *vs* Ag/AgCl, in which was obtained an amorphous and uniform film on the FTO substrate. After annealing, the photoanode exhibited a photocurrente of 20 µA cm^{-2} at 1.23 V *vs* RHE in 0.1 mol L^{-1} KH_2PO_4 pH 7, but after FeOOH photodeposition the photocurrent reached to 1.6 mA cm^{-2}. Also, electrochemical deposition has been used to obtain molybdenum-doped $BiVO_4$. This was demonstrated by Park et al. [40] who added Mo(VI) precursor to a solution containing $Bi(NO_3)_3$ and $VOSO_4$. The Mo-doped $BiVO_4$ showed an increase of 100% in the photoactivity compared to pristine $BiVO_4$. Similarly, Pihosh et al. [28] carried out the potentiostatic deposition, but they used a two-electrode configuration at 55 °C and applied 0.21 V *vs* a Pt counter electrode on a

Table 1
Main methods used to produce heterojunction based on $WO_3/BiVO_4$.

WO_3 layer deposition	$BiVO_4$ layer deposition	Ref
Solvothermal/HT	Spin-coating/HT	[20]
Spin-coating/HT	Spin-coating/HT	[21–25]
Glancing angle deposition	Glancing angle deposition/HT	[26]
Oblique angle deposition/HT	Drop-casting/HT	[27]
Glancing angle deposition/ HT	**ED** of amorphous $BiVO_4$/HT	[28]
Anodizing/HT	Spin-coating/HT	[29]
Doctor Blade/HT	Spin-coating/HT	[30]
Drop-casting/HT	Drop-casting/HT	[31,32]
Electrospining/HT	Dip-coating/HT	[33]
Solvothermal to produce Bi_2WO_6	HT in tube furnace with $V(C_5H_7O_2)_3$	[34]
E-beam/Solvothermal/HT	**ED** of amorphous $BiVO_4$/HT	[35]
ASCVD/HT	Spin-coating/HT	[36]
Solvothermal/HT	SILAR deposition/HT	[37]
Spin-coating/Solvothermal/ HT	Spin-coating/HT	[38]
Spin-coating/HT/ Solvothermal/HT	Spin-coating/HT	[24]
Spray/HT	**ED** of metallic Bi/Drop-casting of NH_3VO_3/HT to produce pillar structure of $BiVO_4$	this work

ED = Electrodeposition; ASCVD = Aerosol assisted chemical vapour deposition; HT = Heat Treatment.

WO_3 nanorod working electrode. Thereby, they obtained the WO_3-nanorods/$BiVO_4$ heterojunction after heat treatment at 500 °C for 2 h. The authors employed the heterojunction in a photoelectrochemical-solar cell tandem device that achieved 8.1% solar-to-hydrogen efficiency. A different approach to $BiVO_4$ electrodeposition was proposed by Dall'Antonia et al. [41], in which it was electrochemically deposited a metallic Bi on the substrate. Then, the substrate was transferred to a solution containing $NaVO_3$, and the Bi film was anodically stripped to generate Bi(III) and induce the in situ precipitation of $BiVO_4$ on the substrate. The photoanode presented a photocurrent of ca. 0.5 mA cm^{-2} at 1.23 V *vs* RHE under non-standard illumination (full output of a 100 W tungsten halogen lamp).

In most $BiVO_4$ electrochemical deposition methods, the production of the stoichiometric oxide is obtained in at least three stages. First is the electrodeposition of one metallic precursor. Second is heat conversion to $BiVO_4$ with the addition of the other metallic precursor. The final step is the dissolution of the contaminations. This is the strategy employed by McDonald et al. [42] and Kim et al. [43], in which BiOI is electrodeposited on FTO by the reduction of *p*-benzoquinone. The *p*-benzoquinone reduction consumed H^+ ions, which elevated the local pH and triggered the precipitation of BiOI on the substrate. After that, the BiOI is converted to $BiVO_4$ by dropping of vanadium precursor on BiOI and annealing. Lastly, the excess V_2O_5 is dissolved with 1 mol L^{-1} NaOH. The BiOI electrodeposition step was used to increase the surface area of the photoanode due to its characteristic crystallization. The BiOI precipitates as two-dimensional plate-like crystals. Lee et al. [44] proposed a modification of the BiOI electrodeposition process to improve the nucleation density of the crystals and to reduce the deposition current density of the growth step. Thus, the electrodeposition was made in two steps: first -0.35 V *vs* Ag/AgCl for 20 s and second -0.10 V *vs* Ag/AgCl for 17 min. On the other hand, Zhong et al. [45] employed the electrodeposition of bismuth oxide as an intermediary step to produce $BiVO_4$ in presence of *p*-benzoquinone as additive during the electrodeposition. After that, the bismuth oxide is converted to $BiVO_4$ by dropping of vanadyl acetylacetonate and heat treatment. The authors related photocurrents of 1.6 and 4.5 mA cm^{-2} approximately for $BiVO_4$ and $BiVO_4/CoO_x/NiO$, respectively.

Aiming to increase the surface area and porosity of the $BiVO_4$ photoanodes, Kang et al. [46] performed the electrodeposition of metallic Bi on FTO in non-aqueous solution (ethylene glycol) at -1.8 V *vs*

Ag/AgCl. They were searching for a dendritic deposit, which could increase the porosity of the final photoanode. Afterwards, the dendritic Bi was converted to $BiVO_4$ by dropping vanadium precursor on Bi film and annealing. Also, Kim et al. [47] electrodeposited metallic Bi in dimethylsulfoxide followed by its conversion to $BiVO_4$ by dropping of vanadyl acetylacetonate solution onto Bi film and annealing at 450 °C for 3 h. The $BiVO_4$ films presented high porosity due to the dendritic morphology of the electrodeposited metallic Bi. In contrast, Wang et al. [48,49] potentiostatically deposited Bi_2O_3 on FTO by applying 2.82 V *vs* RHE for 1.5 h using an electrolyte containing $Bi(NO_3)_3$, acetic acid, and HNO_3. Furthermore, the Bi_2O_3 was converted to $BiVO_4$ by dropping of vanadyl acetylacetonate onto Bi_2O_3 film and annealing at 500 °C for 2 h, thereafter the $BiVO_4$ film shows a compact and uniform morphology.

Here, we propose electrodeposition of metallic Bi on a WO_3 planar film to improve the heterojunction and obtain the dendritic $BiVO_4$ after the dripping of NH_4VO_3 on electrodeposited Bi and annealing at 500 °C. The electrodeposition could enhance the junction between the semiconductors to produce a staggered gap heterostructure, which will increase the charge separation. Both semiconductors were produced using inexpensive techniques, since the WO_3 is made by spray deposition while the $BiVO_4$ is obtained by Bi electrodeposition followed by its conversion in the presence of NH_4VO_3 and heat treatment.

2. Experimental section

2.1. Preparation of WO_3 film

The WO_3 layer on FTO (Fluorine-doped tin oxide coated glass, surface resistivity $\approx$ 8 Ω cm^{-2}, 3 mm thick with a 545 nm thick FTO layer, TEC 8®) was deposited by spray coating using an airbrush (BC 61–03, Forusi®) with 10 L min^{-1} and 3 mL min^{-1} of air and solution flows, respectively. The time of spray was 1 s and the substrate was kept at 100 °C. The precursor solution was $(NH_4)_{10}H_2(W_2O_7)_6$ 0.002 mol L^{-1} dissolved in a mix of ethylene glycol:H_2O 1:1 (V:V). An time interval of 1 min was kept between each spray deposition, and after 10 repetitions the substrates were heat-treated at 500 °C for 60 min.

2.2. Bi electrodeposition on WO_3 film

The Bi was electrodeposited in a three-electrode configuration cell using the WO_3 film, Pt foil, and Ag/AgCl/KCl saturated (Ag/AgCl) as the working, counter, and reference electrodes, respectively. The electrolyte consisted of 0.02 mol L^{-1} $Bi(NO_3)_3$ + 0.1 mol $NaClO_4$ mol L^{-1} dissolved in poly(ethylene glycol) 300 (PEG-300) (Kollisolv®). The choice of a non-aqueous solvent was based on the need to obtain nanostructured morphologies without the competitive reaction of hydrogen evolution during metal deposition. Besides, the previous study showed that the use of PEG 300 in the preparation of $BiVO_4$ photoanodes gave good photoactivity results due to its effect on the oxide crystallization parameters [50]. The Bi electrodeposition was performed at room temperature with magnetic stirring and applying −1.85 V *vs* Ag/AgCl limited with a deposition charge of −50 mC cm^{-2} by pulse.

2.3. Addition of NH_4VO_3 and thermal conversion from Bi to $BiVO_4$

For the production of $BiVO_4$, 50 μL cm^{-2} of 0.1 mol L^{-1} NH_4VO_3 was dropped onto electrodeposited Bi, which was heat-treated at 500 °C for 60 min with a heating rate of 2 °C min^{-1}. Afterwards, the excess of V_2O_5 was dissolved by immersion of the photoanode into 1.0 mol L^{-1} NaOH for 3 min. The photoanode was washed with a copious amount of water.

2.4. Characterizations

The crystalline structure of the samples was investigated by X-ray diffraction (XRD-diffractometer XRD-6000, Shimadzu®, Cu kα irradiation, λ = 1.54 Å, continuous scan, step 0.02°, scan rate 0.5° min^{-1}, receiving slit 0.3 mm). The morphology was characterized by high-resolution field emission scanning electron microscopy (FE-SEM, Zeiss Supra 35 at 5 kV). The optical properties were studied by diffuse reflectance spectroscopy using a UV–Vis-NIR spectrophotometer coupled with an integrating sphere (DRS, Cary 5G, Varian®). The photoanodes were characterized by RAMAN microspectroscopy with an exposure time of 30 s and an accumulation of 100 spectra (532 nm He-Cd laser, 50 mW, coupled to an Olympus BX41 microscope and CCD detector, Horiba HR 550 spectrometer).

The PEC characterizations were carried out in a three-electrode cell with the photoanodes, Pt foil, and Ag/AgCl as the working, counter, and reference electrodes, respectively. Electrical measurements were performed using a potentiostat/galvanostat (PGSTAT302N, Autolab, Methrom®). The light source was an LCS-100 Solar Simulator (Xenon lamp 100 W, filter AM 1.5G, irradiance of 100 mW cm^{-2}, model 94011A-ES, Newport®). The electrolyte was 0.1 mol L^{-1} Na_2HPO_4 + 0.5 mol L^{-1} Na_2SO_4, pH 7.0. The pH of the electrolyte was adjusted with 3.0 mol L^{-1} H_3PO_4. All measurements were carried out at room temperature. The Ag/AgCl electrode potential was converted to RHE by the Nernst equation:

$$E_{RHE} = E_{Ag/AgCl} + E^{\circ}_{Ag/AgCl} + (0.059 \times pH) \qquad (1)$$

where E_{RHE} is the potential *vs* RHE, $E^{\circ}_{Ag/AgCl}$ is 0.197 V at 25 °C, $E_{Ag/AgCl}$ is the potential *vs* Ag/AgCl measured and pH is 7.0.

The transient absorption spectroscopy (TAS) measurements were performed at a μs-s time scale using a pump–probe transient absorption spectrometer (Optical Building Blocks Corporation – OBB). The pump source was a nitrogen laser excitation (337 nm, pulse width of 6 ns, 1 Hz repetition, 150 μJ cm^{-2} $pulse^{-1}$); while the probe source was a tungsten lamp source at the wavelength of 450 nm selected using an OBB monochromator. The measurements were carried out in the same three-electrode cell described in the PEC characterization. The transient absorption change (mΔOD) was measured using a digital oscilloscope (TDS 2022C, Tektronic®).

3. Results and discussion

The microscopy images in Fig. 1 show a homogeneous and compact WO_3 film on the FTO substrate. This feature is important in the formation of the heterojunction, because it is essential for deposition of the $BiVO_4$ layer on WO_3 and not directly on FTO. This configuration inhibits the formation of alternative paths for the photogenerated charge carriers across the photoanode and enables an effective spatial separation of the electron-hole pairs when the charge is transferred from one layer to another [10]. The deposition of metallic Bi on the WO_3 layer has a dendritic morphology with structures distributed along the surface of the substrate. Two aspects of the Bi electrodeposition lead to the dendritic morphology: the high viscosity of PEG-300 and the overpotential of −1.90 V used in the procedure (Supplementary information S1). PEG-300 has a viscosity 100 times higher than water. Therefore, the diffusion of Bi(III) in the solution is slow when compared to an aqueous solution. Besides, under high overpotential, the deposition process is mass transport-controlled and the dendritic deposit is favored [51,52]. The XRD pattern of Bi electrodeposited shows a rhombohedral metallic Bi without a preferential growth (Supplementary Information S2). The same dendritic morphology was observed by Bilican et al. [52], but the authors used an aqueous medium. This Bi morphology drives the shape of the $BiVO_4$. Consequently, after heat treatment in the presence of NH_4VO_3, pillar-like structures of $BiVO_4$ are observed (Fig. 1c and d). Obtaining this type of pillar-like structure with the metallic Bi electrodeposition is quite
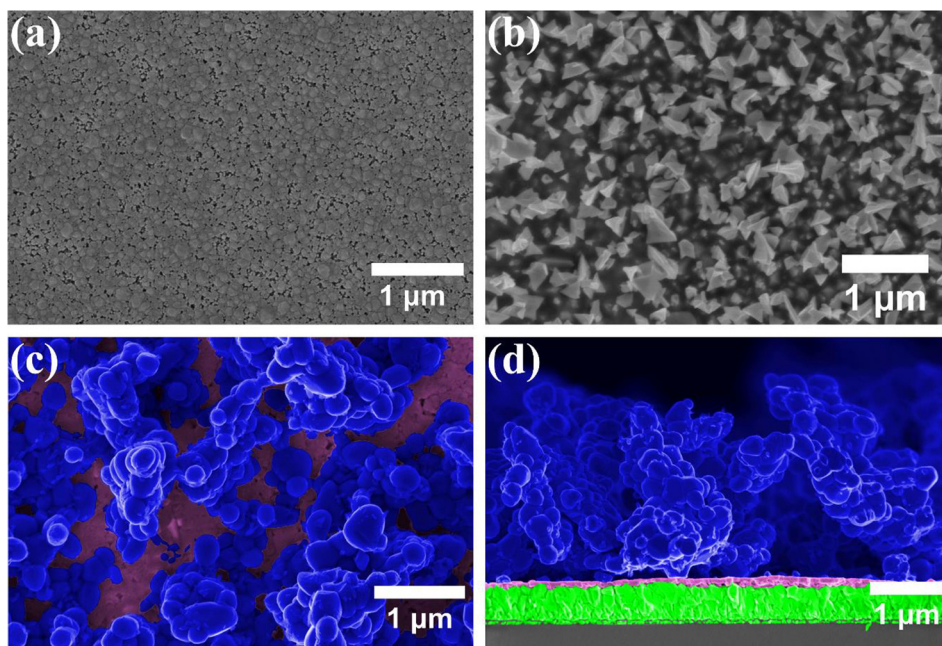
Fig. 1. SEM images of (a) WO_3, (b) Bi metallic on WO_3, (c) $BiVO_4$ on WO_3 after heat treatment with NH_4VO_3 and dissolution of the excess V_2O_5 with 1.0 mol L^{-1} NaOH and (d) cross-section of the photoanode showing the FTO, WO_3 and $BiVO_4$ layers. The colors in Fig. 1c and 1d are an artifice for a better understanding of the layers of the compounds. Blue represents the $BiVO_4$ deposit, WO_3 magenta, and green the FTO substrate.

interesting, since it increases the active area of the photoanode, which is attractive for water splitting. The analyses of the thickness of the layers in the image of Fig. 1d show thicknesses of 545 ± 34 nm for the FTO layer and 92 ± 27 nm for the WO_3 thin film and the height of the pillar-like structures of $BiVO_4$ is 2490 ± 490 nm. Yoon et al. [53] investigated the pillar-like structures of $BiVO_4$ by employing electrospray deposition, and they showed that there was an improvement in the photoactivity of the photoanode, which was assigned to the high surface area of the pillar-like structures $BiVO_4$ film compared to planar electrodes.

Although the pillar-like structure of $BiVO_4$ is an interesting aspect, the absence of physical contact of these structures with the WO_3 layer may indicate resistance to charge transfer between the $BiVO_4$ and WO_3 layer. In any case, the contact break may have been caused by a fracture of the sample used to obtain the cross-section image. This hypothesis seems to be the most plausible, since the $WO_3/BiVO_4$ heterojunction shows a significant increase in the photocurrent when compared to photoanodes containing WO_3 or $BiVO_4$, which will be shown later.

Fig. 2a shows the X-ray diffractogram of the $WO_3/BiVO_4$ photoanode, which presents characteristic diffraction peaks for both triclinic WO_3 and monoclinic $BiVO_4$ phases. The three diffraction peaks observed at 23.2, 23.7, and 24.4° are characteristic of the triclinic WO_3 phase (JPDS 20–1323). Monoclinic $BiVO_4$ presents characteristic peaks at 15.2, 18.8, 19.0, and 30.7° (JPDS 14-688). In addition, there is no preferential growth for WO_3 or $BiVO_4$. The absence of diffraction peaks of V_2O_5 demonstrated that the immersion of the photoanode in 1.0 mol L^{-1} NaOH for the dissolution of excess V_2O_5 was effective. Moreover, the band gap energy calculated is in agreement with the crystalline phases observed in the X-ray diffractograms of WO_3 and $BiVO_4$. The lattice planes of WO_3 and $BiVO_4$ are shown in the Tables S2-2 and S2-3 in the Supplementary Information S2. The Tauc plots shown in Fig. 2b present an indirect bandgap of 2.78 eV for pristine WO_3 film, while the heterojunction $WO_3/BiVO_4$ exhibited a direct bandgap of 2.45 eV, which is expected for monoclinic $BiVO_4$ [54,55]. The observation of only one bandgap for the heterojunction is related to the $BiVO_4$ film thickness and the technique used to determine this optical property. Since the height of the pillar-like structures (film thickness) is on the order of 2.0 μm, all incident radiation is absorbed by the $BiVO_4$ layer, and little radiation with a wavelength below 506 nm is reflected to the detector in the diffuse reflectance integration sphere. In these circumstances, only the bandgap of the outermost layer is observed, in this

case the $BiVO_4$ layer.

The Raman scattering spectra for the WO_3 and $WO_3/BiVO_4$ samples are shown in Fig. 2c. Characteristic scattering peaks for WO_3 are observed at 130, 264, 322, 704, and 801 cm^{-1} [54,56]. The intense peaks at 704 and 801 cm^{-1} correspond to the stretching and angular deformation vibrations of the W−O−W bond. The peaks at 264 and 322 cm^{-1} refer to the angular vibration modes of the O−W−O bonds, while the peak at 130 cm^{-1} is related to crystal lattice vibration. For $BiVO_4$, the scattering peaks are observed at 122, 203, 325, 359, 707, and 817 cm^{-1}. These correspond to the network vibration modes (122 and 203 cm^{-1}), angular deformations of the VO_4^{3-} (325 and 359 cm^{-1}), and stretching at V−O bonds (707 and 817 cm^{-1}) [57].

The photographic images of the resulting photoanodes after each production step are shown in Fig. S3-1 (Supplementary Information S3). The WO_3 film is translucent and it exhibits the expected electrochromic effect under polarization at −1.85 V *vs* Ag/AgCl. Thus, the charge cut-off limiting the Bi deposition of −50 mC cm^{-2} per pulse refers to the sum of the reduction of the WO_3 film itself and the reduction of Bi^{3+} to metallic Bi. The electrochromic effect exhibited by WO_3 is related to two associated effects, the electron accumulation in surface states near the conduction band and the charge compensation by the insertion of ions into interstitial sites with the respective formation of tungsten bronze as M_xWO_3 (with M = H^+, Li^+ or Na^+ and × ≤ 1) [58].

Aiming at the application of the photoanode in water photo-electrooxidation, all of the deposition processes were optimized according to the photocurrent obtained in experiments under simulated sun illumination (Xenon lamp 100 W, AM 1.5G filter, 100 mW cm^{-2}). As shown in Fig. 3a, the photocurrent obtained at 1.23 V *vs* RHE increases as the number of WO_3 spray deposition steps increases. This was expected due to the WO_3 presenting an indirect bandgap, which makes thicker layers necessary to increase the absorption of incident radiation. However, in Fig. 3b, this tendency is not observed for the heterostructure. Fig. 3b exhibits the linear voltammograms under chopped illumination for the heterostructures obtained with 100 (red line) and with 40 (black line) layers of WO_3 spray deposition, WO_3-100L/$BiVO_4$, and WO_3-40L/$BiVO_4$, respectively. In both heterostructures, the $BiVO_4$ was produced from 10 pulses of Bi electrodeposition with a delay of 2 min between the pulses keeping the electrochemical cell under open circuit potential and magnetic stirring. It is noteworthy that the pulsed Bi electrodeposition (Bi-PED) was chosen because this method shows a
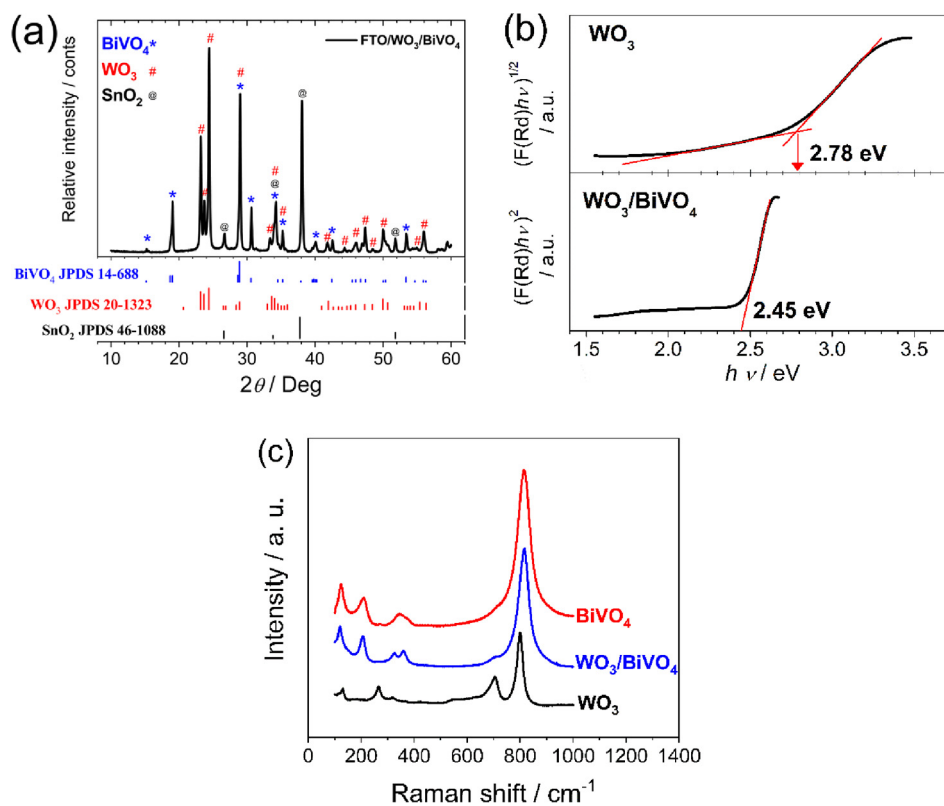
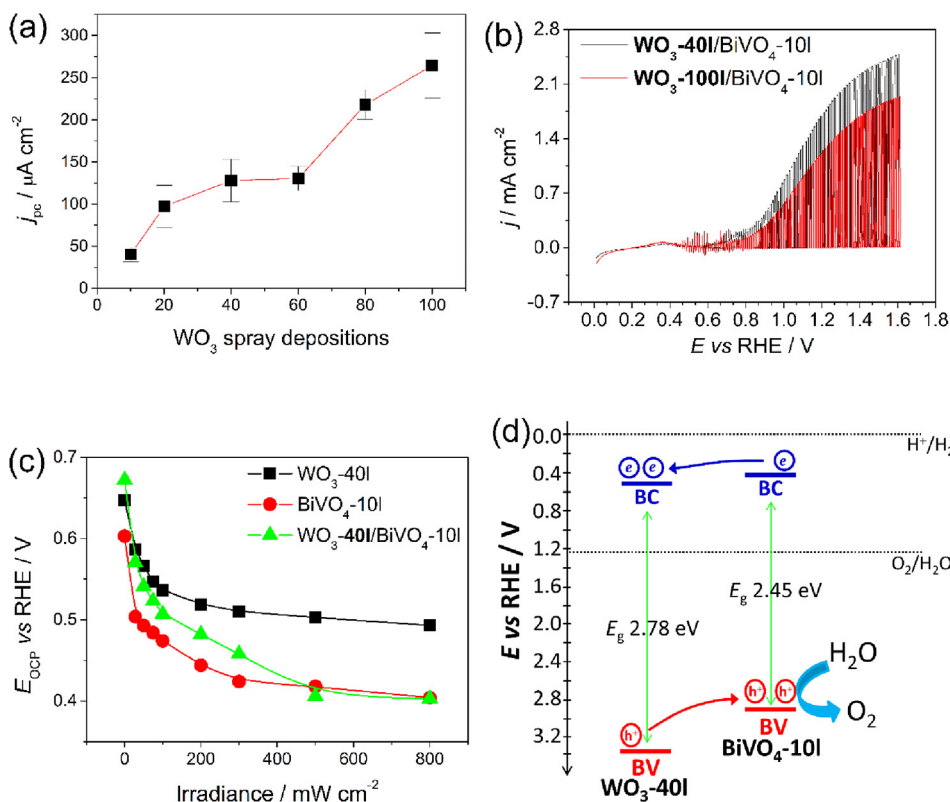**Fig. 2.** (a) XRD of WO_3/$BiVO_4$ photoanode, (b) Tauc plot and (c) Ramam spectra of WO_3, $BiVO_4$ and WO_3/$BiVO_4$ photoanode.

Fig. 3. (a) Photocurrent as a function of WO_3 deposition steps. (b) Linear voltammetry at 5 mV s^{-1} of WO_3-40 L/$BiVO_4$ and WO_3-100 L/$BiVO_4$ showing the effect of the WO_3 deposition steps on photocurrent under chopped light (frequency of 1 Hz). (c) Illuminated open circuit potential as function of irradiance. (d) Representation of the band levels of the semiconductors. The measurements were performed in 0.5 mol L^{-1} Na_2SO_4 + 0.1 mol L^{-1} phosphate buffer pH 7.

photocurrent 275% higher than the continuous Bi electrodeposition (Bi-CED); under the same charge density of Bi electrodeposition (Supplementary Information S4). The conversion from metallic bismuth to $BiVO_4$ with drop-casting of NH_4VO_3 and heat treatment was the same in both methods, Bi-PED and Bi-CED. As evidenced by voltammograms in the Fig. 3b, the photoanode with the highest photocurrent response was obtained with 40 layers of WO_3 spray deposition. Thus, we decided to optimize the photo-electrodeposition of Bi by keeping 40 layers of WO_3 spray deposition. The heterojunctions obtained by less WO_3 spray depositions showed lower photocurrents, because the coating of FTO was not uniform, which made the heterojunction inefficient.

To determine the conduction (CB) and valence (VB) band positions of the semiconductors, as well as their flat band potentials (E_{fb}), the illuminated open circuit potential ($E_{OCP-illuminated}$) was investigated under different radiation intensities. When a semiconductor is illuminated with a radiation source with energy higher than its bandgap, an electron-hole pair is produced, and the electron is excited to the CB while the hole remains in the VB. However, since the system is kept at an open circuit, there is no charge flow, and the photogenerated electrons are accumulated in the depletion region. As a result, when the intensity of radiation increases, the photogenerated charge production and the charge accumulation increases too. This accumulation of charges causes the gradual unfolding of CB and VB until the illumination intensity is high enough to make them fully unfolded, reaching E_{fb}.

Since the $E_{OCP-illuminated}$ is monitored as the radiation intensity increases, the E_{fb} and the type of the semiconductor material can be determined. The E_{fb} is assumed to be the potential where the $E_{OCP-illuminated}$ vs. irradiance intensity plot reaches a stationary plateau under high irradiance intensities, while the semiconductor type is determined by the behavior of the curve. More precisely, if the $E_{OCP-illuminated}$ decreases under illumination, the semiconductor will be n-type. Otherwise, if the $E_{OCP-illuminated}$ increases under illumination, the semiconductor is p-type. If the E_{fb} of the material is known, it could be assumed that its potential is approximately the potential of CB for n-type or VB for p-type semiconductors. Once the position of one of the band levels has been determined, the other band potential can be calculated according to the bandgap energy (E_g) of the material [59]. Thus, in agreement with Fig. 3c, the WO_3 and $BiVO_4$ are both n-type semiconductors, and their CB levels are around 0.49 and 0.40 V vs RHE, while their VB levels are 3.27 and 2.85 V vs RHE, as the representation in Fig. 3d shows.

The CB levels for both semiconductors are more positive than the thermodynamic potential for proton reduction, which is expected. This means that neither WO_3 nor $BiVO_4$ are suitable for photoreduction of water without applied bias [17,60–63]. According to the band levels, the $WO_3/BiVO_4$ produces a heterostructure of type-II with the CB and VB levels of WO_3 more positive than $BiVO_4$ [10]. Such a band configuration easily drives the electron transfer from $BiVO_4$ to WO_3, while the holes cannot be transferred to WO_3. Instead, the holes can only drive towards the photoanode-electrolyte interface. This charge transport prevents electron-hole recombination, because it promotes a spatial charge separation [63].

The number of cycles of Bi pulsed electrodeposition on the WO_3 layer was investigated, and the photocurrent density (j_{pc}) obtained for electrodes from 10 to 50 cycles is shown in Fig. 4a. It is noteworthy that the experiments were performed by applying 1.23 V vs RHE to the photoanode in 0.5 mol L^{-1} Na_2SO_4 + 0.1 mol L^{-1} Na_2HPO_4 pH 7.0 solution under illumination (100 mW cm^{-2}, Xenon lamp 100 W, AM 1.5G filter) for 3 min. The j_{pc} was determined by the difference in the current obtained with the photoanode in the dark and under illumination after 3 min. Although the highest j_{pc} was observed with the photoanode obtained with 10 cycles of Bi pulsed electrodeposition, it was also the one with the highest j_{pc} deviation. This is due to the fact that these photoanodes have a non-uniform surface coating during the metallic Bi deposition step. This non-uniform coating means that after conversion to $BiVO_4$, it will still have a non-uniform coating. However, when the largest amount of Bi was deposited, the photocurrent decreased drastically, showing that the recombination of electron-hole pairs increases significantly in these cases. Thus, a balance must be achieved between the cycles of Bi deposition and the uniformity of the coating. Here, we chose to keep 10 cycles of Bi deposition, because we are interested in as much photocurrent as possible. Fig. 4b shows the linear voltammograms of the photoanodes containing the pristine semiconductors compared to heterojunction under the optimized conditions. It can be observed that the photocurrent obtained with the photoanode $WO_3/BiVO_4$ (2.27 mA cm^{-2}) is 25 times higher than that observed for pristine WO_3 (0.09 mA cm^{-2}) or $BiVO_4$ (0.07 mA cm^{-2}). This significant increase in photocurrent is due to the effective spatial separation of electron-hole pairs, which increases the water oxidation rate. To the best comparison with some recent results of literature with photoanodes based on $WO_3/BiVO_4$ heterojunction is shown in the Table S5-1 in the Supplementary Information S5.

Up to this point, we have observed an appreciable improvement in the photocurrent density obtained by the $WO_3/BiVO_4$ heterojunction when compared to the pristine materials, which may be assumed to be a consequence of the better charge separation. To evaluate the charge carrier dynamics and give support to this hypothesis, transient absorption spectroscopy (TAS) was performed on WO_3, $BiVO_4$, and $WO_3/BiVO_4$ photoanodes. Fig. 5a shows the mΔOD values as a function of the probe-light wavelength (550–900 nm) in the presence or absence of applied bias. In the present study, no absorption signal was detected at wavelength values lower than 550 nm. The first noticeable feature is the dependence of the mΔOD values on the wavelength of the probe light. In all cases, the maximum absorption was reached at 650 nm, the wavelength at which holes were monitored. It is perceptible that the $WO_3/BiVO_4$ heterojunction photoanode has a much higher mΔOD signal compared to the individual semiconductors, indicating more effective charge separation. In agreement with Ma et al. [64,65] and Selim et al. [36], the photogenerated holes are the absorbent species in this range of wavelength for the WO_3 and $BiVO_4$. Since the maximum absorption value was at 650 nm, this wavelength was set to monitor the kinetics of the photogenerated holes' decay as a function of the applied
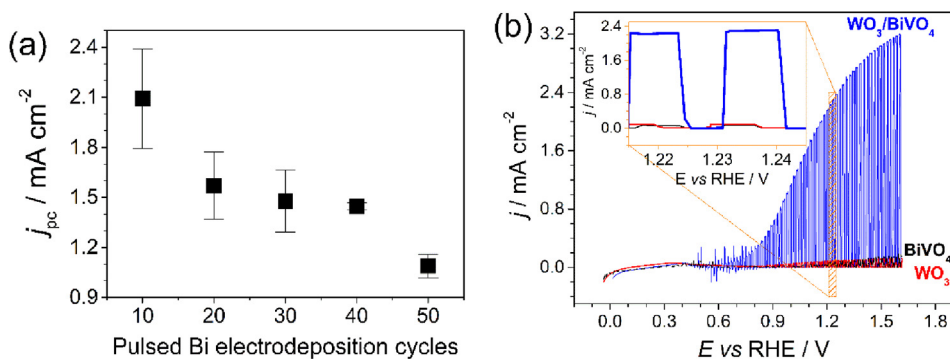

Fig. 4. (a) Photocurrent as function of the cycles of pulsed electrodeposition of Bi on WO_3–40L. (b) Linear voltammetry at 5 mV s^{-1} to WO_3-40L (red line), $BiVO_4$-10L (black line) and WO_3-40L/$BiVO_4$-10L (blue line) under chopped light with simulated solar light into 0.5 mol L^{-1} Na_2SO_4 + 0.1 mol L^{-1} Na_2HPO_4 pH 7.0 solution. (For interpretation of the references to colour in this figure legend, the reader is referred to the web version of this article.)
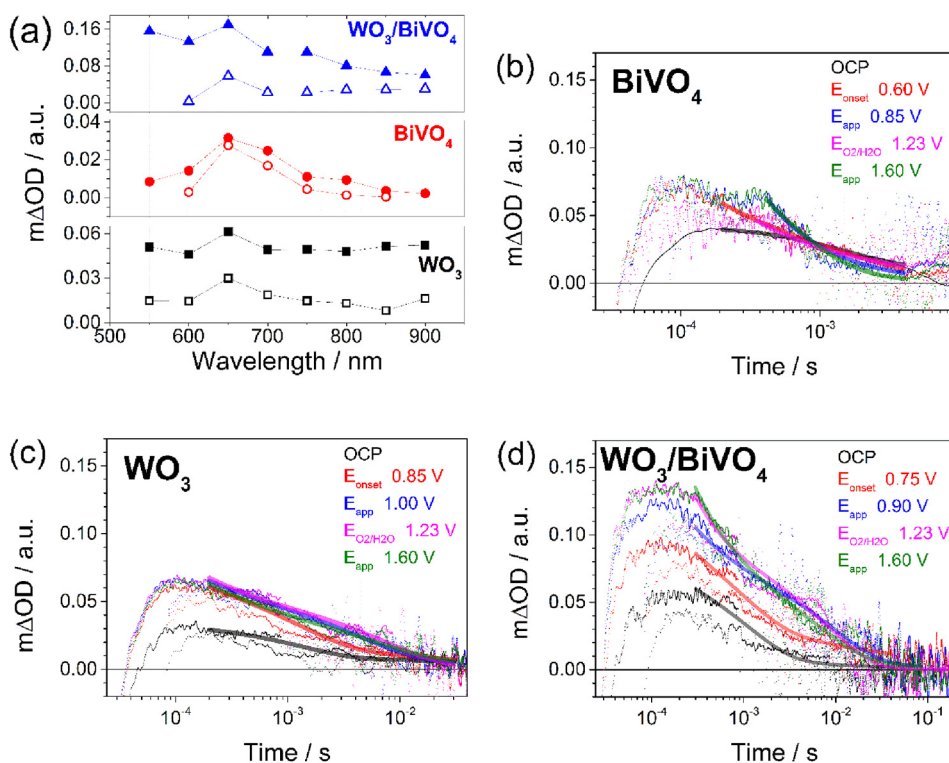
Fig. 5. (a) Transient absorption spectra in 0.1 mol L^{-1} phosphate buffer + 0.1 mol L^{-1} Na$_2$SO$_4$ recorded at 200 μs after laser excitation (337 nm, 150 μJ cm^{-2} pulse^{-1}, 1 Hz). Transient absorption kinetic decays of (b) BiVO$_4$ and (c) WO$_3$ pristine photoanodes, and (d) WO$_3$/BiVO$_4$ heterojunction. The applied potentials are (black) OCP, (red) E_{onset} to photocurrent, (blue) intermediary bias between OCP and reversible water oxidation, (magenta) 1.23 V *vs* RHE, and (green) high overpotential of 1.6 V *vs* RHE. The solid lines are the fitting. (For interpretation of the references to colour in this figure legend, the reader is referred to the web version of this article.)

potential.

To determine the applied potential range in the transient absorption decays, the photoelectrochemical activity of the photoanodes was measured under the same electrochemical conditions. However, an incident monochromatic light source at 450 nm was used. At this wavelength, the energy is higher than the bandgap of the WO$_3$ and BiVO$_4$ semiconductors and therefore capable of generating electron-hole pairs. The linear voltammograms are shown in Fig. S6-1 (Supplementary information S6). The open-circuit potentials (OCP), the onset potentials (E$_{onset}$) of photocurrents, and the photocurrent at the reversible potential of water oxidation (E$_{O2/H2O}$) in the experimental conditions are highlighted in the voltammograms. The chosen potentials aimed to evaluate the transient absorption decay behavior according to the applied potential. In all measurements, it was observed that the mΔOD values were lower under OCP conditions (no bias) compared to the experiments under applied bias (Fig. 5b-d).

The power-law associated with exponential decay of the transient absorption was used to fit the data and to obtain the time constant (τ) of the decay. The equation used for fitting was the same as the one used by Ma et al. [64,65] and Selim et al. [36] and the kinetic model is considers the transient absorption decay to be a first-order reaction (Supplementary information S7). The consideration of a first-order reaction is in agreement with the data shown by Ma et al. [66]. They found that a change in the order reaction from first- to third-order only occurred when the hole density at the surface was higher than 1 hole nm^{-2}, which was reached at higher photocurrent densities. The τ values at the ms timescale of the transient absorption decays are shown in Fig. 6. The increase in the τ values as a function of the applied potential is observed only for the WO$_3$ and WO$_3$/BiVO$_4$ photoanodes. This behavior is associated with the charge carrier mobility and the diffusion length and with the charge recombination kinetics of the materials. The charge carriers diffusion length and mobility of BiVO$_4$ are both shorter than that of WO$_3$–charge carriers' diffusion lengths of 60–100 [67,68] and 75–500 nm [9,69] respectively; the charge carriers' mobilities are ~ 10^{-2} [70] and ~ 5 cm^2 V^{-1} s^{-1} [69], respectively. Consequently, the effective charge separation in BiVO$_4$ is lower than in WO$_3$ due to the highest charge recombination for the former. Hence, BiVO$_4$
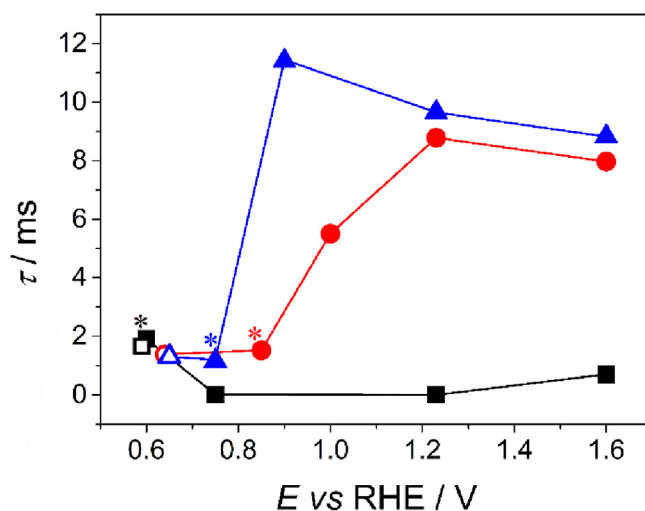

Fig. 6. Time constant (τ) as a function of applied potential for photoanodes in agreement with the power-law decay associated with an exponential decay fitting. BiVO$_4$ (squares), WO$_3$ (circles), and WO$_3$/BiVO$_4$ (triangles). The empty symbols are the τ calculated under OCP and the asterisk identify the E$_{onset}$ of photocurrent.

presents lower τ values than WO$_3$. On the other hand, in the heterostructure, the WO$_3$ underlayer works as a charge separator for the electrons photogenerated at the BiVO$_4$ top layer after the incidence of the pulsed laser. Thus, the photogenerated charges are efficiently separated by decreasing the charge recombination rate and increasing the τ value. The external bias works as a driving force for the charge flow, which increases the charge transport and consequently the τ values. For a pristine BiVO$_4$ photoanode, no increase in the τ value is observed upon increasing the applied bias, because charge recombination is dominant for BiVO$_4$.

The high values of τ for the WO$_3$/BiVO$_4$ heterojunction and the surface area are in agreement with the high photocurrent observed for the heterojunction. The formation of the heterostructure is the main
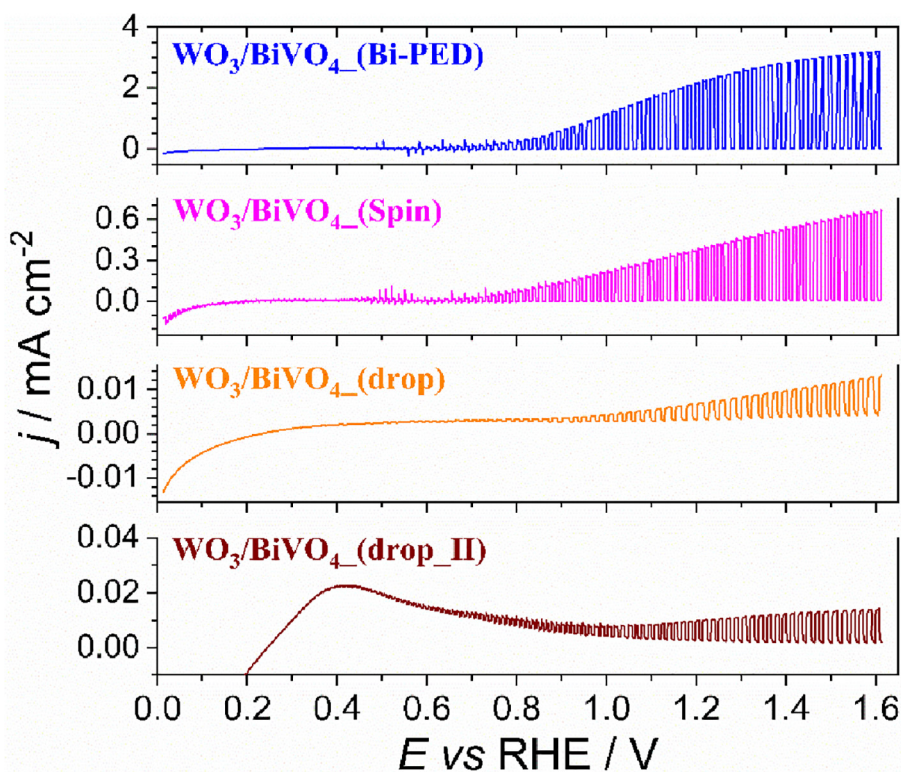
Fig. 7. Linear voltammograms at 5 mV s^{-1} obtained with heterojunctions produced by Bi electrodeposition, spin-coating and by drop-casting using different solution compositions. The experiments were performed in Na$_2$SO$_4$ 0.5 mol L^{-1} + Na$_2$HPO$_4$ 0.1 mol L^{-1} pH 7.0 under solar simulated illumination.

reason for the increase in the photoactivity of the photoanode, notwithstanding, the pillar-like structure also contributes to enhance its performance. It is believed that the pillar-like structure works as an antireflective coverage and the reaction of water oxidation occurs faster near to the interface between WO$_3$/BiVO$_4$ (at the base of the BiVO$_4$ pillars) than on top of BiVO$_4$ structures. However, it is hard to accuracy the region where the reaction take place without an in situ technique for evaluation.

The most impressive observation is the effect of the BiVO$_4$ deposition method on the photocurrent density by comparing heterojunctions produced by the previous Bi electrodeposition step with those obtained by drop-casting and spin-coating (Supplementary Information S8). Fig. 7 shows that the heterojunction obtained by the previous Bi electrodeposition (WO$_3$/BiVO$_4$_Bi-PED) is ca. 300 times higher than that obtained by drop-casting methods, that is, (i) using a BiVO$_4$ suspension (WO$_3$/BiVO$_4$_(drop)) or (ii) using a Bi(NO$_3$)$_3$ solution to produce a BiO$_x$ layer followed by use of NH$_4$VO$_3$ solution to produce a V$_x$O$_y$ layer (WO$_3$/BiVO$_4$_(drop_II)). It is worth mentioning that the volume used in a drop of the BiVO$_4$ suspension was estimated to be similar to the quantity of Bi electrodeposited, considering the charge pass during the electrodeposition step. As the spin-coating is the technique mostly used for the BiVO$_4$ deposition, here the photoanodes were produced based on the methodology proposed by Selim et al. [36] (Supplementary Information S8). The heterojunction produced by the previous Bi electrodeposition step is ca. 6 times higher than that by spin-coating (WO$_3$/BiVO$_4$_(spin)). It is clear that the Bi electrodeposition is important in order to guarantee the formation of a suitable junction between the WO$_3$ and BiVO$_4$ layer.

Another way to demonstrate the increase of the charge separation efficiency (η_{sep}) is the study of photo electrochemical behavior of the photoanodes in presence of a hole scavenger. So, the influence of Bi pre-step electrodeposition to build the heterojunction with 100% of catalytic efficiency (η_{cat}) was evaluated using sodium sulfite [43,55]. The η_{sep} and η_{cat} were determined by using the Eq. (2), where j_{H_2O} is the photocurrent density measured and j_{abs} is the photon absorption rate

expressed as current density. The j_{abs} is calculated assuming 100% of absorbed photon-to-current efficiency and was determined from the light harvesting efficiency (LHE) of the WO$_3$/BiVO$_4$ heterojunction and pristine WO$_3$ and BiVO$_4$ photoanodes (The details are available in Supplementary Information S9) [71].

$$j_{H_2O} = j_{abs} \times \eta_{sep} \times \eta_{cat} \qquad (2)$$

The j_{abs} calculated were 2.074, 0.864 and 4.487 mA cm^{-2} to BiVO$_4$, WO$_3$ and heterojunctions WO$_3$/BiVO$_4$, respectively. In Table 2 are shown the parameters obtained from the analysis of the photocurrents generated in the presence and absence of sodium sulfite (Supplementary Information S10), from which η_{cat} and η_{sep} are calculated as follow:

$$\eta_{sep} = \frac{j_{Na_2SO_3}}{j_{abs}} \qquad (3)$$

$$\eta_{cat} = \frac{j_{H_2O}}{j_{Na_2SO_3}} \qquad (4)$$

In Fig. 8 are shown the η_{sep} and η_{cat} at 1.23 V *vs* RHE calculated to the photoanodes produced from different methodologies. Among all methods, the best performance is showed by the heterojunction produced with the pre-step Bi pulsed electrodeposition (Bi-PED) on WO$_3$.

Table 2
Photocurrents obtained from the experiments in the presence and absence of Na$_2$SO$_3$.

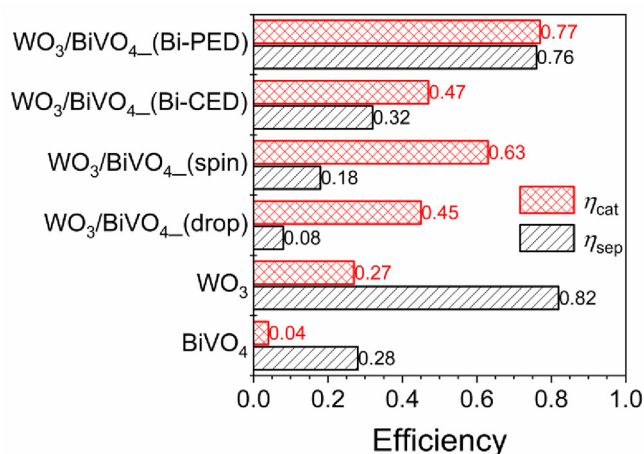| Photoanode	j_{H_2O} (mA cm^{-2})	$j_{Na_2SO_3}$ (mAcm^{-2})
BiVO$_4$	0.025	0.574
WO$_3$	0.195	0.711
WO$_3$/BiVO$_4$_(drop)	0.163	0.363
WO$_3$/BiVO$_4$_(spin)	0.517	0.816
WO$_3$/BiVO$_4$_(Bi-CED)	0.668	1.425
WO$_3$/BiVO$_4$_(Bi-PED)	2.595	3.390

Fig. 8. Charge separation and catalytic efficiencies at 1.23 V *vs* RHE for heterojunctions produced on WO_3 film by pre-step Bi pulsed electrodeposition ($WO_3/BiVO_4\_(PED)$); pre-step Bi continuous electrodeposition ($WO_3/BiVO_4\_(CED)$); spin-coating of $BiVO_4$ precursor solution ($WO_3/BiVO_4\_(spin)$); dropping-casting of $BiVO_4$ precursor solution ($WO_3/BiVO_4\_(drop)$); and for pristine photoanodes WO_3 and $BiVO_4$.

In fact, is demonstrated that the Bi-PED is better than continuous electrodeposition (Bi-CED) on WO_3, once that the η_{sep} and η_{cat} are both highest to the former. The η_{sep} observed is 0.76 while the η_{cat} is 0.77 to the $WO_3/BiVO_4\_(Bi-PED)$. Although the pristine WO_3 present a highest η_{sep} (0.82) its η_{cat} is very low (0.27). Furthermore, this data are in agreement with the TAS decay study, in which it is observed high time constant for the heterojunction and the WO_3 pristine electrode. In addition, in Fig. S10-1 is shown the voltammetric profiles of the photoanodes into 0.1 mol L^{-1} sodium phosphate buffer pH 7.0 containing 1.0 mol L^{-1} Na_2SO_3 (Supplementary Information S10). In all profiles are observed an increase of the photocurrent under illumination and presence of the Na_2SO_3. However, in low bias, the increment of photocurrent is larger than at high bias. Despite of this, the heterojunction $WO_3/BiVO_4\_(Bi-PED)$ shows the smaller improvement at high bias (Supplementary Information S10, Fig. S10-2).

We believe that the Bi electrodeposition begins with an epitaxial growth, which assures a certain degree of crystalline continuity in the first atomic layers. In agreement with the electrodeposition theory, this process is the cumulative effect of ionic transport, discharge, nucleation, and growth. Besides, the growth of electrodeposits can be compared to growth from the vapor phase. However, the mechanism of growth is strongly influenced by the crystalline characteristics of the substrate surface, such as large number of grains with different orientations, vacancies, dislocations, and adsorbed molecules [72,73]. The electrodeposit growth on polycrystalline substrates is associated with the formation of two- or three-dimensional nuclei, and its first stage is the deposition of isolated adatoms and subsequent clustering. The clusters become stable when they reach a critical size and act as nucleation centers. The formation of a monolayer is completed as more adatoms join the stable clusters, and the repetition of this process leads to the growth of the next layer over the newly grown monolayer. This mechanism of electrochemical epitaxial growth is supported by the works of Bao and Kavanagh [74,75] and Svedberg et al. [76] about Bi and Fe epitaxial electrodeposition on GaAs(1 1 1).

As the growth mechanism by the cluster formation is repeated and the thickness of the electrodeposit increases, mismatches arise due to the presence of defects in the substrate; then epitaxial growth is lost. Anyway, in the locus of contact between the substrate and the electrodeposits, the electrodeposition could ensure better crystalline continuity and band alignment. Therefore, this study shows that electrodeposition control of the overlay could be used to improve the photoactivity of the materials by the enhancement of heterojunction growth.

The stability of the photoanodes was performed during 2 h of solar simulated illumination and it is observed a decrease in the photocurrent for all photoanodes (Supplementary Information S11). The $WO_3/BiVO_4$ heterojunction keeps 54% of the initial photocurrent at 1.23 V *vs* RHE (1.16 mA cm^{-2}), while the pristine WO_3 becomes non-photoactive after 1 h and the $BiVO_4$ increase its photocurrent from 87 to 130 µA cm^{-2}. It is believed that there is leaching of the WO_3 layer from the FTO due to the pH of the electrolyte. In agreement with Nave et al. [77], at WO_3 is soluble and yields WO_4^{2-} ions at pH 7. Regarding the $BiVO_4$ stability in the conditions of the experiment, Toma et al. [78] show a chemical instability associated to attack of its surface under aqueous solution. This instability is accelerated by illumination, high pH, and applied anodic bias. The illumination affects the stability of $BiVO_4$ due to the accumulation of holes at its surface, which destabilize the lattice of the crystals and cause the dissolution of the material. We believe that the decreasing in the photocurrent is result of the dissolution of the underneath WO_3 layer in addition to partially attack at the surface of $BiVO_4$. The alternative to minimize the photo corrosion of the heterojunction is the deposition of protective layers as Al_2O_3, which is stable under the electrolyte pH and applied bias conditions [79]. Another possibility is the change in the electrolyte composition, as demonstrated by Lee et al. [53], which used an electrolyte of 1 M potassium borate buffer pH 9.3 saturated with V_2O_5. The V(V) soluble in solution is incorporated at the oxygen evolution catalysts (FeOOH/NiOOH), nevertheless, the authors point out that further studies are required to better understand the changes provided by the vanadium addition.

4. Conclusions

The WO_3 spray deposition proved to be very effective for producing a uniform and adherent layer with excellent thickness control. This feature allowed the formation of heterojunctions with $BiVO_4$ that presented excelent results for water splitting. An average current of 2.1 ± 0.3 mA cm^{-2} at 1.23 V *vs* RHE (Xenon lamp, AM1.5G, 100 mW cm^{-2}) was reached, which is 35 and 23 times higher than $BiVO_4$ and WO_3 pristine electrodes, respectively. The electrodeposition of metallic Bi prior to its conversion to $BiVO_4$ enabled the formation of pillar-like structures that contributed to an increase of the electroactive area due to nano-texturing of the surface. Interestingly, there is no correlation to the photocurrent data and the WO_3 layer thickness in the pristine photoanodes and in the heterojunction. For the WO_3 pristine photoanodes as highest the number of spray depositions highest the photocurrent. However, for the heterojunctions, when the number of Bi electrodeposition on WO_3 layers is the same, the photocurrent observed to the heterojunction containing 40 sprayed layers of WO_3 is higher than that containing 100 sprayed layers of WO_3.

Regarding the $BiVO_4$ deposition, it was observed that the use of a preceding metallic Bi electrodeposition step ensures a better heterojunction with the WO_3 layer and consequently the highest photocurrent. This is more evident when the photoactivity of the heterojunction produced by the previous Bi electrodeposition step is compared with those produced by the drop casting and spin-coating methods for the water oxidation reaction. The former presents an increase of ca. 300 times in relation to drop-casting and 6 times if compared to spin-coating methods. In addition, it was possible to observe the effective formation of a heterojunction and its effect on the charge carriers separation, which is effectively increased after the formation of staggered gap heterostructure (type-II) with a time constant of approximately 10 ms under an applied potential of 1.23 V *vs* RHE. However, an increase in the time constant for $WO_3/BiVO_4$ and WO_3 photoanodes was observed when the applied potential was higher than the potential of onset photocurrent. We believe that this occurs due to the photoactivation of the WO_3 layer, which provides more efficient charge transport than the $BiVO_4$. The use of electrodeposition as a tool for the production of heterojunctions appears to be an effective method

for the improvement of the junction between two different semiconductors. Since this technique is inexpensive, scalable, and easy to operate, the dissemination of electrodeposition can open new perspectives for the production of photoanodes and photocathodes for water division.

Declaration of Competing Interest

The authors declare that they have no known competing financial interests or personal relationships that could have appeared to influence the work reported in this paper.

Acknowledgements

The authors thank the Proof-Reading-Service.com by the proofing of the paper.

Funding

Appendix A. Supplementary data

Supplementary data to this article can be found online at https://doi.org/10.1016/j.cej.2020.125836.

References

[1] Z. Chen, T.F. Jaramillo, T.G. Deutsch, A. Kleiman-Shwarstein, A.J. Forman, N. Gaillard, R. Garland, K. Takanabe, C. Heske, M. Sunkara, E.W. McFarland, K. Domen, E.L. Milled, H.N. Dinh, Accelerating materials development for photoelectrochemical hydrogen production: Standards for methods, definitions, and reporting protocols, J. Mater. Res. 25 (2010) 3–16 https://doi:10.1557/jmr.2010.0020.

[2] M.W. Kanan, D.G. Nocera, In situ formation of an oxygen-evolving catalyst in neutral water containing phosphate and Co2 +, Science 321 (5892) (2008) 1072–1075, https://doi.org/10.1126/science.1162018.

[3] M.H.V. Huynh, T.J. Meyer, Proton-coupled electron transfer, Chem. Rev. 107 (2007) 5004–5064, https://doi.org/10.1021/cr0500030.

[4] T.A. Betley, Q. Wu, T. Van Voorhis, D.G. Nocera, Electronic design criteria for O − O Bond formation via metal − oxo complexes, Inorg. Chem. 47 (2008) 1849–1861 https://doi:10.1021/ic701972n.

[5] K. Sayama, A. Nomura, Z. Zou, R. Abe, Y. Abe, H. Arakawa, Photoelectrochemical decomposition of water on nanocrystalline BiVO4 film electrodes under visible light, Chem. Commun. 3 (2003) 2908–2909 https://doi:10.1039/b310428a.

[6] L.H. Mascaro, A. Pockett, J.M. Mitchels, L.M. Peter, P.J. Cameron, V. Celorrio, D.J. Fermin, J.S. Sagu, K.G.U. Wijayantha, G. Kociok-Köhn, F. Marken, One-step preparation of the BiVO4 film photoelectrode, J. Solid State Electrochem. 19 (2014) 31–35 https://doi:10.1007/s10008-014-2495-y.

[7] J.K. Cooper, S. Gul, F.M. Toma, L. Chen, P.A. Glans, J. Guo, J.W. Ager, J. Yano, I.D. Sharp, Electronic structure of monoclinic BiVO4, Chem. Mater. 26 (2014) 5365–5373 https://doi:10.1021/cm5025074.

[8] Y. Park, K.J. McDonald, K.S. Choi, Progress in bismuth vanadate photoanodes for use in solar water oxidation, Chem. Soc. Rev. 42 (2013) 2321–2337 https://doi:10.1039/c2cs35260e.

[9] M.A. Butler, Photoelectrolysis and physical properties of the semiconducting electrode WO2, J. Appl. Phys. 48 (1977) 1914–1920 https://doi:10.1063/1.323948.

[10] S.J.A. Moniz, S.A. Shevlin, D.J. Martin, Z.X. Guo, J. Tang, Visible-light driven heterojunction photocatalysts for water splitting-a critical review, Energy Environ. Sci. 8 (2015) 731–759 https://doi:10.1039/c4ee03271c.

[11] J.T. Calow, P.J. Deasley, S.J.T. Owen, P.W. Webb, A review of semiconductor heterojunctions, J. Mater. Sci. 2 (1967) 88–96 https://doi:10.1007/BF00550056.

[12] J.M. Langer, H. Heinrich, Deep-level impurities: A possible guide to prediction of band-edge discontinuities in semiconductor heterojunctions, Phys. Rev. Lett. 55 (1985) 1414–1417 https://doi:10.1103/PhysRevLett.55.1414.

[13] J. Tersoff, Theory of semiconductor heterojunctions: The role of quantum dipoles, Phys. Rev. B 30 (1984) 4874–4877 https://doi:10.1103/PhysRevB.30.4874.

[14] X. Li, J. Yu, J. Low, Y. Fang, J. Xiao, X. Chen, Engineering heterogeneous semiconductors for solar water splitting, J. Mater. Chem. A 3 (2015) 2485–2534 https://doi:10.1039/c4ta04461d.

[15] S.K. Choi, W. Choi, H. Park, Solar water oxidation using nickel-borate coupled

[16] C. Martinez Suarez, S. Hernández, N. Russo, BiVO4 as photocatalyst for solar fuels production through water splitting: A short review, Appl. Catal. A Gen. 504 (2015) 158–170.

BiVO4 photoelectrodes, PCCP 15 (2013) 6499–6507 https://doi:10.1039/c3cp00073g.

[17] H. Wang, L. Zhang, Z. Chen, J. Hu, S. Li, Z. Wang, J. Liu, X. Wang, Semiconductor heterojunction photocatalysts: Design, construction, and photocatalytic performances, Chem. Soc. Rev. 43 (2014) 5234–5244 https://doi:10.1039/c4cs00126e.

[18] M. Tayebi, B.K. Lee, Recent advances in BiVO4 semiconductor materials for hydrogen production using photoelectrochemical water splitting, Renew. Sustain. Energy Rev. 111 (2019) 332–343 https://doi:10.1016/j.rser.2019.05.030.

[19] B.S. Kalanoor, H. Seo, S.S. Kalanur, Recent developments in photoelectrochemical water-splitting using WO3/BiVO4 heterojunction photoanode: A review, Mater. Sci. Energy Technol. 1 (2018) 49–62 https://doi:10.1016/j.mset.2018.03.004.

[20] J. Su, L. Guo, N. Bao, C.A. Grimes, Nanostructured WO3/BiVO4 heterojunction films for efficient photoelectrochemical water splitting, Nano Lett. 11 (2011) 1928–1933 https://doi:10.1021/nl2000743.

[21] H.W. Jeong, T.H. Jeon, J.S. Jang, W. Choi, H. Park, Strategic modification of BiVO4 for improving photoelectrochemical water oxidation performance, J. Phys. Chem. C 117 (2013) 9104–9112 https://doi:10.1021/jp400415m.

[22] I. Fujimoto, N. Wang, R. Saito, Y. Miseki, T. Gunji, K. Sayama, WO3/BiVO4 composite photoelectrode prepared by improved auto-combustion method for highly efficient water splitting, Int. J. Hydrogen Energy 39 (2014) 2454–2461 https://doi:10.1016/j.ijhydene.2013.08.114.

[23] I. Grigioni, K.G. Stamplecoskie, E. Selli, P.V. Kamat, Dynamics of Photogenerated Charge Carriers in WO3/BiVO4 Heterojunction Photoanodes, J. Phys. Chem. C 119 (2015) 20792–20800 https://doi:10.1021/acs.jpcc.5b05128.

[24] I. Rodríguez-Gutiérrez, E. Djatoubai, J. Su, A. Vega-Poot, G. Rodríguez-Gattorno, F.L. Souza, G. Oskam, An intensity-modulated photocurrent spectroscopy study of the charge carrier dynamics of WO3/BiVO4 heterojunction systems, Sol. Energy Mater. Sol. Cells 208 (2020) 110378 https://doi:10.1016/j.solmat.2019.110378.

[25] I. Grigioni, M.V. Dozzi, E. Selli, Photoinduced electron transfer in WO3/BiVO4 heterojunction photoanodes: Effects of the WO3 layer thickness, J. Phys.: Condens. Matter 32 (2020), https://doi:10.1088/1361-648X/ab440b.

[26] Y. Pihosh, I. Turkevych, K. Mawatari, T. Asai, T. Hisatomi, J. Uemura, M. Tosa, K. Shimamura, J. Kubota, K. Domen, T. Kitamori, Nanostructured WO 3/BiVO 4 photoanodes for efficient photoelectrochemical water splitting, Small 10 (2014) 3692–3699 https://doi:10.1002/smll.201400276.

[27] X. Shi, I.Y. Choi, K. Zhang, J. Kwon, D.Y. Kim, J.K. Lee, S.H. Oh, J.K. Kim, J.H. Park, Efficient photoelectrochemical hydrogen production from bismuth vanadate-decorated tungsten trioxide helix nanostructures, Nat. Commun. 5 (2014) 1–8 https://doi:10.1038/ncomms5775.

[28] Y. Pihosh, I. Turkevych, K. Mawatari, J. Uemura, Y. Kazoe, S. Kosar, K. Makita, T. Sugaya, T. Matsui, D. Fujita, M. Tosa, M. Kondo, T. Kitamori, Photocatalytic generation of hydrogen by core-shell WO3/BiVO4 nanorods with ultimate water splitting efficiency, Sci. Rep. 5 (2015) 1–2 https://doi:10.1038/srep11141.

[29] L. Xia, J. Bai, J. Li, Q. Zeng, X. Li, B. Zhou, A highly efficient BiVO4/WO3/W heterojunction photoanode for visible-light responsive dual photoelectrode photocatalytic fuel cell, Appl. Catal. B Environ. 183 (2016) 224–230 https://doi:10.1016/j.apcatb.2015.10.050.

[30] S.Y. Chae, C.S. Lee, H. Jung, O.S. Joo, B.K. Min, J.H. Kim, Y.J. Hwang, Insight into charge separation in WO3/BiVO4 heterojunction for solar water splitting, ACS Appl. Mater. Interfaces 9 (2017) 19780–19790 https://doi:10.1021/acsami.7b02486.

[31] J.H. Seo, G. Park, K.H. Oh, S.H. Kang, H.C. Lee, S.K. Cho, K.M. Nam, Analysis of charge separation processes in WO3-BiVO4 composite for efficient photoelectrochemical water oxidation, J. Electroanal. Chem. 789 (2017) 17–23 https://doi:10.1016/j.jelechem.2017.02.021.

[32] S.J. Hong, S. Lee, J.S. Jang, J.S. Lee, Heterojunction BiVO4/WO3 electrodes for enhanced photoactivity of water oxidation, Energy Environ. Sci. 4 (2011) 1781–1787 https://doi:10.1039/c0ee00743a.

[33] S. Xu, D. Fu, K. Song, L. Wang, Z. Yang, W. Yang, H. Hou, One-dimensional WO3/BiVO4 heterojunction photoanodes for efficient photoelectrochemical water splitting, Chem. Eng. J. 349 (2018) 368–375 https://doi:10.1016/j.cej.2018.05.100.

[34] Y. Zhou, L. Zhang, L. Lin, B.R. Wygant, Y. Liu, Y. Zhu, Y. Zheng, C.B. Mullins, Y. Zhao, X. Zhang, G. Yu, Highly efficient photoelectrochemical water splitting from hierarchical WO3/BiVO4 nanoporous sphere arrays, Nano Lett. 17 (2017) 8012–8017 https://doi:10.1021/acs.nanolett.7b04626.

[35] J.H. Kim, D.H. Kim, J.W. Yoon, Z. Dai, J.H. Lee, Rational design of branched WO3 nanorods decorated with bivo4 nanoparticles by all-solution processing for efficient photoelectrochemical water splitting, ACS Appl. Energy Mater. 2 (2019) 4535–4543 https://doi:10.1021/acsaem.9b00776.

[36] S. Selim, L. Francàs, M. García-Tecedor, S. Corby, C. Blackman, S. Gimenez, J.R. Durrant, A. Kafizas, WO3/BiVO4: Impact of charge separation at the timescale of water oxidation, Chem. Sci. 10 (2019) 2643–2652 https://doi:10.1039/c8sc04679d.

[37] V.S. Kumbhar, H. Lee, J. Lee, K. Lee, Interfacial growth of the optimal BiVO4 nanoparticles onto self-assembled WO3 nanoplates for efficient photoelectrochemical water splitting, J. Colloid Interface Sci. 557 (2019) 478–487 https://doi:10.1016/j.jcis.2019.09.037.

[38] Y. Liu, B.R. Wygant, K. Kawashima, O. Mabayoje, T.E. Hong, S.-G. Lee, J. Lin, J.-H. Kim, K. Yubuta, W. Li, J. Li, C.B. Mullins, Facet effect on the photoelectrochemical performance of a WO3/BiVO4 heterojunction photoanode, Appl. Catal. B Environ. 245 (2019) 227–239 https://doi:10.1016/j.apcatb.2018.12.058.

[39] J.A. Seabold, K.S. Choi, Efficient and stable photo-oxidation of water by a bismuth vanadate photoanode coupled with an iron oxyhydroxide oxygen evolution

catalyst, J. Am. Chem. Soc. 134 (2012) 2186–2192 https://doi:10.1021/ja209001d.

[40] Y. Park, D. Kang, K.S. Choi, Marked enhancement in electron-hole separation achieved in the low bias region using electrochemically prepared Mo-doped BiVO4 photoanodes, PCCP 16 (2014) 1238–1246 https://doi:10.1039/c3cp53649a.

[41] L.H. Dall'Antonia, N.R. De Tacconi, W. Chanmanee, H. Timmaji, N. Myung, K. Rajeshwar, Electrosynthesis of bismuth vanadate photoelectrodes, Electrochem. Solid-State Lett. 13 (2010) 29–32.

[42] K.J. McDonald, K.S. Choi, A new electrochemical synthesis route for a BiOI electrode and its conversion to a highly efficient porous BiVO 4 photoanode for solar water oxidation, Energy Environ. Sci. 5 (2012) 8553–8557 https://doi:10.1039/c2ee22608a.

[43] T.W. Kim, K.S. Choi, Nanoporous BiVO4 photoanodes with dual-layer oxygen evolution catalysts for solar water splitting, Science 343 (80) (2014) 990–994, https://doi.org/10.1126/science.1246913.

[44] D.K. Lee, K.S. Choi, Enhancing long-term photostability of BiVO4 photoanodes for solar water splitting by tuning electrolyte composition, Nat. Energy 3 (2018) 53–60 https://doi:10.1038/s41560-017-0057-0.

[45] M. Zhong, T. Hisatomi, T. Minegishi, H. Nishiyama, M. Katayama, T. Yamada, K. Domen, Bulky crystalline BiVO4 thin films for efficient solar water splitting, J. Mater. Chem. A 4 (2016) 9858–9864 https://doi:10.1039/c6ta03072f.

[46] D. Kang, Y. Park, J.C. Hill, K. Choi, Preparation of Bi-based ternary oxide photoanodes BiVO4, Bi2WO6, and Bi2Mo3O12 using dendritic Bi metal electrodes, J. Phys. Chem. Lett. 5 (2014) 2994–2999 https://doi:10.1021/jz501544k.

[47] H.R. Kim, G. Kim, S. Il In, Y. Park, Optimization of porous BiVO4 photoanode from electrodeposited Bi electrode: Structural factors affecting photoelectrochemical performance, Electrochim. Acta 189 (2016) 252–258.

[48] S. Wang, P. Chen, Y. Bai, J.H. Yun, G. Liu, L. Wang, New BiVO4 dual photoanodes with enriched oxygen vacancies for efficient solar-driven water splitting, Adv. Mater. 30 (2018) 1–7 https://doi:10.1002/adma.201800486.

[49] S. Wang, T. He, J.H. Yun, Y. Hu, M. Xiao, A. Du, L. Wang, New iron-cobalt oxide catalysts promoting BiVO4 films for photoelectrochemical water splitting, Adv. Funct. Mater. 28 (2018) 1–10 https://doi:10.1002/adfm.201802685.

[50] F.W.P. Ribeiro, M.F. Gromboni, F. Marken, L.H. Mascaro, Photoelectrocatalytic properties of BiVO4 prepared with different alcohol solvents, Int. J. Hydrogen Energy 41 (2016) 17380–17389 https://doi:10.1016/j.ijhydene.2016.07.159.

[51] M. Yang, Fern-shaped bismuth dendrites electrodeposited at hydrogen evolution potentials, J. Mater. Chem. 21 (2011) 3119–3124 https://doi:10.1039/c0jm03213a.

[52] D. Bilican, J. Fornell, J. Sort, E. Pellicer, Electrochemical synthesis of bismuth particles: Tuning particle shape through substrate type within a narrow potential window, Materials (Basel). 10 (2017) 1–10 https://doi:10.3390/ma10010043.

[53] H. Yoon, M.G. Mali, J.Y. Choi, M.W. Kim, S.K. Choi, H. Park, S.S. Al-Deyab, M.T. Swihart, A.L. Yarin, S.S. Yoon, Nanotextured pillars of electrosprayed bismuth vanadate for efficient photoelectrochemical water splitting, Langmuir 31 (2015) 3727–3737 https://doi:10.1021/acs.langmuir.5b00486.

[54] J. Díaz-Reyes, R. Castillo-Ojeda, M. Galván-Arellano, O. Zaca-Moran, Characterization of WO3 thin films grown on silicon by HFMOD, Adv. Condens. Matter Phys. 2013 (2013), https://doi:10.1155/2013/591787.

[55] F.F. Abdi, N. Firet, R. vandeKrol, Efficient BiVO4 thin film photoanodes modified with cobalt phosphate catalyst and W-doping, ChemCatChem. 5 (2013) 490–496.

[56] C.V. Ramana, S. Utsunomiya, R.C. Ewing, C.M. Julien, U. Becker, Structural stability and phase transitions in WO3 thin films, J. Phys. Chem. B 110 (2006) 10430–10435 https://doi:10.1021/jp056664i.

[57] J. Yu, A. Kudo, Effects of structural variation on the photocatalytic performance of hydrothermally synthesized BiVO4, Adv. Funct. Mater. 16 (2006) 2163–2169 https://doi:10.1002/adfm.200500799.

[58] M. Regragui, M. Addou, A. Outzourhit, E. El Idrissi, A. Kachouane, A. Bougrine, Electrochromic effect in WO3 thin films prepared by spray pyrolysis, Sol. Energy Mater. Sol. Cells 77 (2003) 341–350 https://doi:10.1016/S0927-0248(02)00353-7.

[59] Z. Chen, H.N. Dinh, E. Miller, Photoelectrochemical Water Splitting, Springer New York, New York, NY, 2013. https://doi:10.1007/978-1-4614-8298-7.

[60] Z.F. Huang, L. Pan, J.J. Zou, X. Zhang, L. Wang, Nanostructured bismuth vanadate-based materials for solar-energy-driven water oxidation: A review on recent progress, Nanoscale 6 (2014) 14044–14063 https://doi:10.1039/c4nr05245e.

[61] H. Pan, Principles on design and fabrication of nanomaterials as photocatalysts for water-splitting, Renew. Sustain. Energy Rev. 57 (2016) 584–601 https://doi:10.1016/j.rser.2015.12.117.

[62] W.T. Qiu, Y.C. Huang, Z.L. Wang, S. Xiao, H.B. Ji, Y.X. Tong, Effective strategies towards high-performance photoanodes for photoelectrochemical water splitting, Acta Phys. - Chim. Sin. 33 (2017) 80–102 https://doi:10.3866/PKU.WHXB201607293.

[63] J.H. Kim, J.S. Lee, BiVO4-based heterostructured photocatalysts for solar water splitting: a review, Energy Environ. Focus. 3 (2014) 339–353 https://doi:10.1166/eef.2014.1121.

[64] Y. Ma, S.R. Pendlebury, A. Reynal, F. Le Formal, J.R. Durrant, Dynamics of photogenerated holes in undoped BiVO4 photoanodes for solar water oxidation, Chem. Sci. 5 (2014) 2964–2973 https://doi:10.1039/c4sc00469h.

[65] Y. Ma, F. Le Formal, A. Kafizas, S.R. Pendlebury, J.R. Durrant, Efficient suppression of back electron/hole recombination in cobalt phosphate surface-modified undoped bismuth vanadate photoanodes, J. Mater. Chem. A 3 (2015) 20649–20657 https://doi:10.1039/c5ta05826k.

[66] Y. Ma, C.A. Mesa, E. Pastor, A. Kafizas, L. Francàs, F. Le Formal, S.R. Pendlebury, J.R. Durrant, Rate law analysis of water oxidation and hole scavenging on a BiVO4 photoanode, ACS Energy Lett. 1 (2016) 618–623 https://doi:10.1021/acsenergylett.6b00263.

[67] J.H. Kim, Y. Jo, J.H. Kim, J.W. Jang, H.J. Kang, Y.H. Lee, D.S. Kim, Y. Jun, J.S. Lee, Wireless solar water splitting device with robust cobalt-catalyzed, dual-doped BiVO4 photoanode and perovskite solar cell in tandem: a dual absorber artificial leaf, ACS Nano 9 (2015) 11820–11829 https://doi:10.1021/acsnano.5b03859.

[68] A.J.E. Rettie, H.C. Lee, L.G. Marshall, J.F. Lin, C. Capan, J. Lindemuth, J.S. McCloy, J. Zhou, A.J. Bard, C.B. Mullins, Combined charge carrier transport and photoelectrochemical characterization of BiVO4 single crystals: Intrinsic behavior of a complex metal oxide, J. Am. Chem. Soc. 135 (2013) 11389–11396 https://doi:10.1021/ja405550k.

[69] R. Lin, J. Wan, Y. Xiong, K. Wu, W.C. Cheong, G. Zhou, D. Wang, Q. Peng, C. Chen, Y. Li, Quantitative study of charge carrier dynamics in well-defined WO3 nanowires and nanosheets: insight into the crystal facet effect in photocatalysis, J. Am. Chem. Soc. 140 (2018) 9078–9082 https://doi:10.1021/jacs.8b05293.

[70] F.F. Abdi, T.J. Savenije, M.M. May, B. Dam, R. Van De Krol, The origin of slow carrier transport in BiVO4 thin film photoanodes: A time-resolved microwave conductivity study, J. Phys. Chem. Lett. 4 (2013) 2752–2757 https://doi:10.1021/jz4013257.

[71] Q. Wu, J. Hou, H. Zhao, Z. Liu, X. Yue, S. Peng, H. Cao, Charge recombination control for high efficiency CdS/CdSe quantum dot co-sensitized solar cells with multi-ZnS layers, Dalt. Trans. 47 (2018) 2214–2221 https://doi:10.1039/c7dt04356b.

[72] R.K. Pandey, S.N. Sahu, S. Chandra, Handbook of semiconductor electrodeposition, Marcel Dekker Inc, New York, 1996 https://doi:10.1201/9781315213989.

[73] M. Stepanova, S. Dew, Nanofabrication, Springer Vienna, Vienna, 2012 https://doi:10.1007/978-3-7091-0424-8.

[74] Z.L. Bao, K.L. Kavanagh, Epitaxial Bi/GaAs(111) diodes via electrodeposition, Appl. Phys. Lett. 88 (2006) 1–3 https://doi:10.1063/1.2161849.

[75] Z.L. Bao, K.L. Kavanagh, Epitaxial Fe/GaAs via electrochemistry, J. Appl. Phys. 98 (2005) 98–101 https://doi:10.1063/1.2014939.

[76] E.B. Svedberg, J.J. Mallett, L.A. Bendersky, A.G. Roy, W.F. Egelhoff, T.P. Moffat, A Structural Study of Electrodeposited Fe on n-GaAs(001), J. Electrochem. Soc. 153 (2006) C807 https://doi:10.1149/1.2353782.

[77] M.I. Nave, K.G. Kornev, Complexity of products of tungsten corrosion: comparison of the 3D pourbaix diagrams with the experimental data, Metall. Mater. Trans. A Phys. Metall. Mater. Sci. 48 (2017) 1414–1424.

[78] F.M. Toma, J.K. Cooper, V. Kunzelmann, M.T. McDowell, J. Yu, D.M. Larson, N.J. Borys, C. Abelyan, J.W. Beeman, K.M. Yu, J. Yang, L. Chen, M.R. Shaner, J. Spurgeon, F.A. Houle, K.A. Persson, I.D. Sharp, Mechanistic insights into chemical and photochemical transformations of bismuth vanadate photoanodes, Nat. Commun. 7 (2016), https://doi:10.1038/ncomms12012.

[79] M.F. Gromboni, D. Coelho, L.H. Mascaro, A. Pockett, F. Marken, Enhancing activity in a nanostructured BiVO4 photoanode with a coating of microporous Al2O3, Appl. Catal. B Environ. 200 (2017) 133–140 https://doi:10.1016/j.apcatb.2016.06.059.